Tseng *et al. Earth, Planets and Space* 2020, **72**(1):161
https://doi.org/10.1186/s40623-020-01283-2

Earth, Planets and Space

EXPRESS LETTER

Anatomy of active volcanic edifice at the Kusatsu–Shirane volcano, Japan, by magnetotellurics: hydrothermal implications for volcanic unrests

Kuo Hsuan Tseng[1], Yasuo Ogawa[2*], Nurhasan[1,3], Sabri Bülent Tank[1,4], Naoto Ujihara[1,5], Yoshimori Honkura[2], Akihiko Terada[2], Yoshiya Usui[1,6] and Wataru Kanda[2]

Abstract

We aimed to perform three-dimensional imaging of the underlying geothermal system to a depth of 2 km using magnetotellurics (MT) at around the Yugama crater, the Kusatsu–Shirane Volcano, Japan, which is known to have frequent phreatic eruptions. We deployed 91 MT sites focusing around the peak area of 2 km × 2 km with typical spacings of 200 m. The full tensor impedances and the magnetic transfer functions were inverted, using an unstructured tetrahedral finite element code to include the topographic effect. The final model showed (1) low-permeability bell-shaped clay cap (C1) as the near-surface conductor, (2) brine reservoir as a deep conductor (C3) at a depth of 1.5 km from the surface, and (3) a vertical conductor (C2) connecting the deep conductor to the clay cap which implies an established fluid path. The columnar high-seismicity distribution to the east of the C2 conductor implies that the flushed vapor and magmatic gas was released from the brine reservoir by breaking the silica cap at the brittle–ductile transition. The past magnetization/demagnetization sources and the inflation source of the 2014 unrest are located just below the clay cap, consistent with the clay capped geothermal model underlain by brine reservoir. The resistivity model showed the architecture of the magmatic–hydrothermal system, which can explain the episodic volcanic unrest.

Keywords: Phreatic eruption, Magnetotelluric method, Clay cap, Brine, Unrest

Introduction

The Kusatsu–Shirane volcano is an active andesitic–dacitic quaternary volcano in Central Japan (Fig. 1a, b). The activity of the volcano started at 0.5–0.6 Ma with magmatic eruptions and pyroclastic flows. After a long dormancy of 0.2–0.3 Ma, magmatic activity restarted from 16 Ka and ended at 1.5 Ka (Terada 2018). The subsequent historically known activities of the Kusatsu–Shirane volcano since 1805 were phreatic eruptions around the peak of the volcano, especially near the Yugama crater (*Y* in Fig. 1c).

Phreatic eruptions are local-scale volcanic phenomena that include explosions of confined volumes of gas and steam, but exclude those directly involved with magma (Stix and de Moor 2018). The cause of phreatic eruptions is related to the changes in transient pressure in the subsurface hydrothermal systems, which is mainly due to the intense temperature increase of shallow aquifers (Kobayashi et al. 2018). A phreatic eruption has a comparatively small impact radius; however, the concentrated gases can be emitted, which spread over a wide area (e.g., Tazieff 1989), and the mechanical energy of eruptions can also provoke fatal ejecta near the crater (e.g.,

*Correspondence: oga@ksvo.titech.ac.jp

[2] Volcanic Fluid Research Center, Tokyo Institute of Technology, Tokyo, Japan
Full list of author information is available at the end of the article

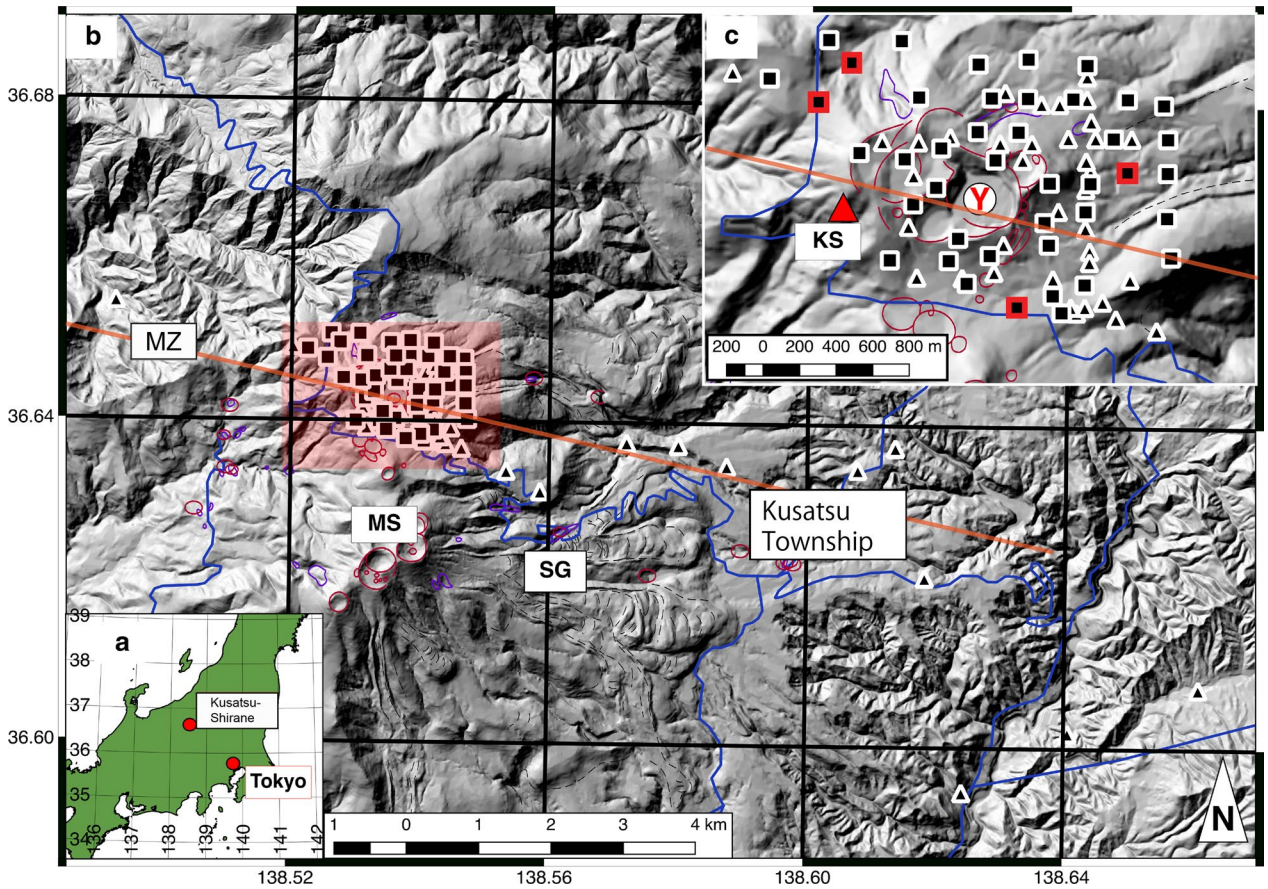

Fig. 1 **a** Location of Kusatsu–Shirane Volcano, Japan. **b** Topography map of Kusatsu–Shirane Volcano with MT/AMT stations. The squares and triangles denote the MT and AMT stations, respectively. The red circles and open curves show the crater rims of past eruptions. The purple closed curves show the fumarole zones. The blue curves show the national road 292 as a location reference. SG, MS, and MZ denote the locations of Sesshougawara fumarolic area, Mt. Motoshirane, and Manza hot spring field, respectively. The long orange line denotes a section in Additional file 2: Figure S23. **c** A peak area [the red rectangle in (**b**)] of Kusatsu–Shirane Volcano with MT/AMT stations. The symbols are the same as in (**b**). Moreover, the black squares with red and with white edges denote the MT station with and without magnetic field data, respectively. KS denotes Mt. Shirane, and the red triangle denotes its peak. Y denotes the Yugama crater lake

Kaneko et al. 2016) or large lahars (e.g., Herd 1986). It is fundamentally important to know the geothermal system underneath the volcano edifice to understand the phreatic eruption mechanism and to mitigate volcanic risks. In this study, we used the magnetotelluric method (MT), an electromagnetic field method, to image the subsurface hydrothermal system in terms of the electrical resistivity, which is sensitive to the distribution of fluids and low-permeability clay cap (e.g., Aizawa et al. 2009; Heise et al. 2008).

The hydrothermal system of the Kusatsu–Shirane volcano has been intensively studied by performing geochemical analysis at the Yugama crater lake and the surrounding fumaroles and hot springs (Sano et al. 1994; Ohba et al. 2019). Ohba et al. (2019) showed a model of a two-phase gas–liquid reservoir underlain by a magmatic fluid reservoir based on the isotope ration of hydrogen and oxygen in relation to recent volcanic unrest.

During the 1990s, which was an active decade in terms of seismicity, peculiar seismic tremor events were monitored, and underlying horizontal crack models with a two-phase reservoir were proposed for the system underneath the Yugama crater (Nakano et al. 2003). However, the overall seismic image of the geothermal system underneath the volcano remains unclear.

Temporal changes due to high-temperature fluid migration were also detected by total magnetic intensity monitoring around the Yugama crater during both active and inactive periods from 1982 to 2012 (Takahashi and Fujii 2014).

For imaging the overall geothermal system, Nurhasan et al. (2006) carried out a 15 km long profiling of

audio-magnetotellurics measurements and showed a two-dimensional resistivity section across the volcano down to a depth of 2 km along the orange line in Fig. 1b, c. Recently, Matsunaga et al. (2020) carried out magnetotelluric measurements 2 km to the south of the Kusatsu–Shirane volcano and showed a three-dimensional structure to a depth of 10 km with 1–2 km horizontal resolutions. Those studies; however, lack detailed site spacings and images of the geothermal system around the active peak area around the Yugama crater. In this study, we focus on the peak area of the Kusatsu–Shirane volcano and will present a three-dimensional resistivity distribution from a densely sampled magnetotelluric data.

Magnetotelluric data

We compiled a dataset consisting of magnetotelluric (MT) and audio-magnetotelluric (AMT) data obtained during 2001–2005. We have 91 sites in total (Fig. 1b, c). See Additional file 1: Table S1 for details. Out of these, 41 sites used an MT system covering a frequency range of 320 Hz–0.5 mHz. Most of them measured only telluric fields onsite, simultaneously with another site with magnetic field measurements (Additional file 1: Table S1). The remaining 50 sites used an AMT system covering a frequency range of 10 kHz–0.1 Hz, which measured two horizontal components of telluric fields and three components of magnetic fields at the same locations. For the MT data which had no magnetic fields (Additional file 1: Table S1), the impedances were calculated using the telluric fields at the site and magnetic fields at another site, assuming that the magnetic fields have a smooth spatial variation. For those impedances using the interstation data (e.g. Martí et al. 2020), the different locations of the telluric, and magnetic fields were considered in the inverse modeling.

In this study, we focus on a 2 km × 2 km area (Fig. 1c) and to a depth of few kilometers in the model interpretations; we also include the NW–SE profile AMT data by Nurhasan et al. (2006) for modeling. We chose 12 frequencies in a range from 320 Hz to 0.1 Hz, which equally spaced in logarithm for inversion. This frequency range could cover the available data in both the MT and AMT measurements.

The observed data are summarized in Fig. 2a as phase tensor ellipses (Caldwell et al. 2004) for 5 representative frequencies. The distribution of ellipses directly shows the directionality and dimensionality of the structure without distortions due to the near-surface anomalies. The ellipses were filled with $\tan^{-1}(\mathbf{\Phi}_2)$, where Φ_2 is the geometric mean of the diagonal components of the phase tensor components ($\Phi_{\max}$ and $\Phi_{\min}$). The Φ_2 phase is a rotational invariant and indicates the changes in electric conductivity with depth. The phases of higher and lower than 45° respectively indicate the existence of more conductive and more resistive bodies with increasing depth. The real and imaginary parts of the induction vectors are also plotted in Fig. 2a for the AMT sites, with Parkinson's convention by which the real vectors point to conductors.

We see more circular-shaped ellipses at higher frequencies, which mean almost one-dimensional resistivity distribution at the near surface. At the frequencies from 70 to 4.4 Hz, the high phase (~75°) spreads around the Yugama crater lake (*Y* in Fig. 2a), and the phases are higher to the east of the Yugama crater. These indicate widespread shallow conductors. The induction vectors point towards the central peak around Yugama lake, which also includes topographic effects. At a frequency of 1.1 Hz, the relatively high-phase area is shifted to the north. The shapes of the ellipses are more circular near the Yugama crater and become more E–W elongated at sites away from the Yugama crater. This feature is an indication of the existence of another deep conductor underneath the Yugama. At a frequency of 0.3 Hz, all the sites show consistent E-W elongated ellipses, which indicate that the peak area has a deep conductor in the N–S strike at depth.

Inverse modeling

We carried out 3-D inversion using impedance data and magnetic transfer function data from 280 to 0.1 Hz. The sites with AMT data utilized impedance data and magnetic transfer function data; Conversely, the sites with MT data utilized only the impedance data (Additional file 1: Table S1). The error floor of impedances was set as 5% of $\sqrt[2]{|\mathbf{Zxy}*\mathbf{Zyx}|}$ (Usui 2015); The error floor of the tipper was set to 0.05 (see Additional file 2: Text S1 for details). As the undulation of the topography has a comparable scale to our target, we used a 3-D inversion code developed by Usui (2015) and Usui et al. (2017), which can incorporate the sharp topography using unstructured tetrahedral meshes. It also allows the inclusion of local galvanic distortions as parameters.

The initial model for the inversion was uniform earth having 100 Ωm resistivity with topography and 10^9 Ωm air. The Yugama crater lake water was modeled with 0.2 Ωm resistivity after the water sample measurement (Terada et al. 2018). The resistivity of the lake water and air was fixed during the iterative calculation. The modeled horizontal electric fields were calculated in such a way that the electric fields were tangential to the ground surface.

The inversion program FEMTIC minimizes the data misfit along with the two constraints, namely the model roughness and the norm of galvanic distortions. Thus, there are two tradeoff hyper-parameters: $\boldsymbol{\alpha}^2$ for model

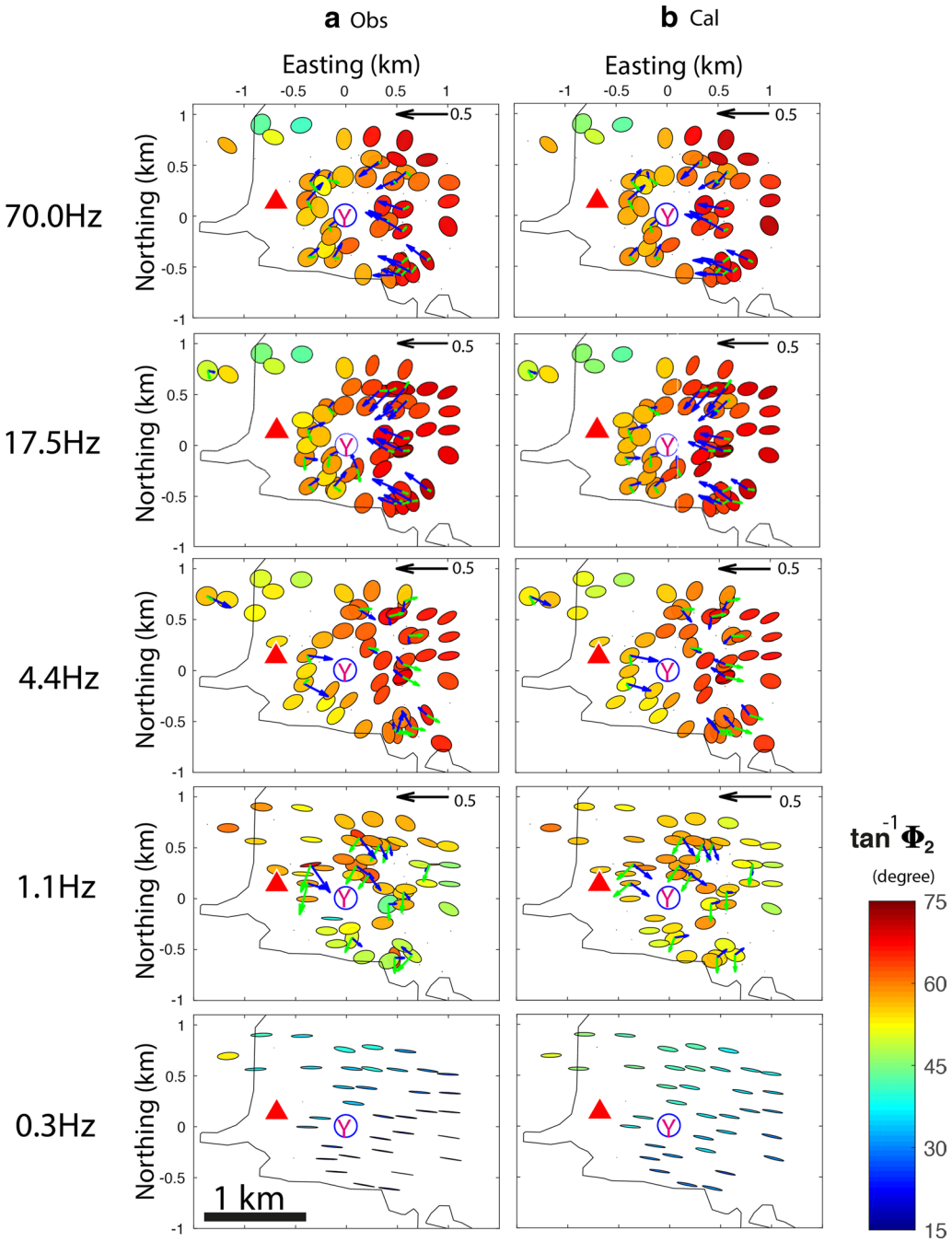

Fig. 2 The phase tensor ellipses map with **a** the observed and **b** the calculated data from the final model. The phase tensor ellipses are filled by $\tan^{-1}\Phi_2$, where Φ_2 is the geometric mean of maximum and minimum of phase tensor. The blue and green arrows show the real and imaginary parts of the induction vectors with Parkinson convention. The black curve, red triangle, and blue circle with Y denote the national road 292, the peak of Mt. Kusatsu–Shirane and the Yugama crater lake, respectively

roughness and $\boldsymbol{\beta}^2$ for the norm of galvanic distortions. We chose a value of $\boldsymbol{\beta}^2$=1 to adequately control the galvanic distortion. For determining the best model, we tested seven different values for $\boldsymbol{\alpha}^2$ (100, 31.6, 10, 3.16, 1, 0.316, and 0.1) and found the best model with $\boldsymbol{\alpha}^2$=1 using the L-curve method (Additional file 2: Figure S1). With the preferred tradeoff parameters, the model converged at the 20th iteration with the root-mean-square (RMS) changes of less than 1% from that of the previous iteration. The RMS decreased from 32.5 to 1.24 from

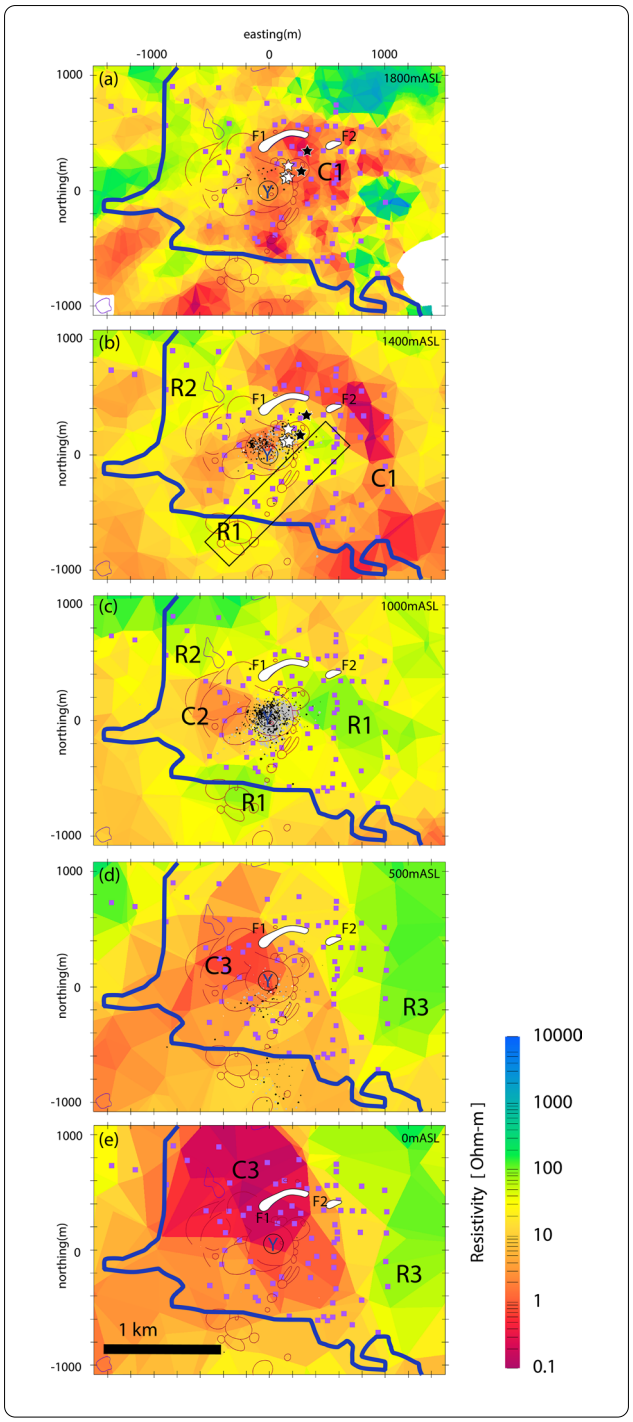

Fig. 3 Depth slices at **a** 1800 m ASL, **b** 1400 m ASL, **c** 1000 m ASL, **d** 500 m ASL and **e** 0 m ASL from the 3-D resistivity inversion at the peak area of Kusatsu–Shirane volcano. Seismic hypocenters are mapped as dots on each map within 200 m tolerance in depth. The white, black, and gray dots denote hypocenters for three periods before, during and after the 2014 unrest, namely from August 2013 to February 2014, from March 2014 to May 2014, and from June 2014 to February 2019. The white and black starts denote horizontal locations of magnetizations and demagnetizations corresponding to volcanic events from 1978 to 2012 after Takahashi & Fujii (2014). The red circles and open curves show the crater rims of past eruptions. The rectangle in (b) denotes the fitting between the resistor R1 and the locations of historical eruptions. Major fumaroles (F1 and F2) are shown by white closed curves

the initial model to the final model. Comparisons of the observed and calculated phase tensors are presented in Fig. 2a, b for five representative frequencies. Both the phase tensor ellipses and its $\mathbf{tan}^{-1}(\mathbf{\Phi}_2)$ phase value show good agreement. The induction vectors also had a reasonable fit. Additional file 1: Table S1 shows the locations of the MT and AMT sites, and the Additional file 2: Figures S2–16 show the comparison of observed and calculated responses for apparent resistivity, impedance phase, and tipper for each site.

Results

The best-fit modeling results are shown as a set of depth slices in Fig. 3. Here we describe the major features of the model.

Figure 3a shows the resistivity distribution at 1800 m above sea level (ASL), which is approximately 400 m below the peak. The area to the east of the Yugama crater is covered with a widespread conductor (C1), which is consistent with the high phase distribution at 70 to 17.5 Hz (Fig. 2). At 1400 m ASL (Fig. 3b), the conductor (C1) still exists but, the resistive anomalies R1 and R2 appear to the southeast and northwest of the area. The C1 shows the semi-circular distribution, and inside the circle, the resistor R1 appears in NE-SW directions and breaking the circular distribution of C1 conductor in the southwestern directions. Interestingly, R1 follows the distributions of the historical phreatic eruption zones from 1902 to 1942 (Terada 2018). At further depth, the circular distribution of C1 is disappearing towards 1000 m ASL (Fig. 3c). The hypocenter of recent seismic activities (see Additional file 2: Text S2 for more details) and magnetization/demagnetization sources (Takahashi and Fujii 2014) are located at the north dge of the R1 resistor. From 1400 to 1000 m ASL, a columnar conductor (C2) is located at the western edge of the Yugama crater. This conductive structure is a newly discovered feature, different from the previous research (e.g., Nurhasan et al. 2006) that we named it C2. There is a seismicity swarm associated with the C2 to the east. At 500 m ASL and below (Figs. 3d, e), a deep conductor (C3) with a resistivity less than 1 Ωm appears in the northwestern part of the area. The Yugama crater is located at the edge of the C3 conductor. The existence of the C3 conductor corresponds to the high phase distribution to the north of the Yugama crater at 1.1 Hz (Fig. 2a).

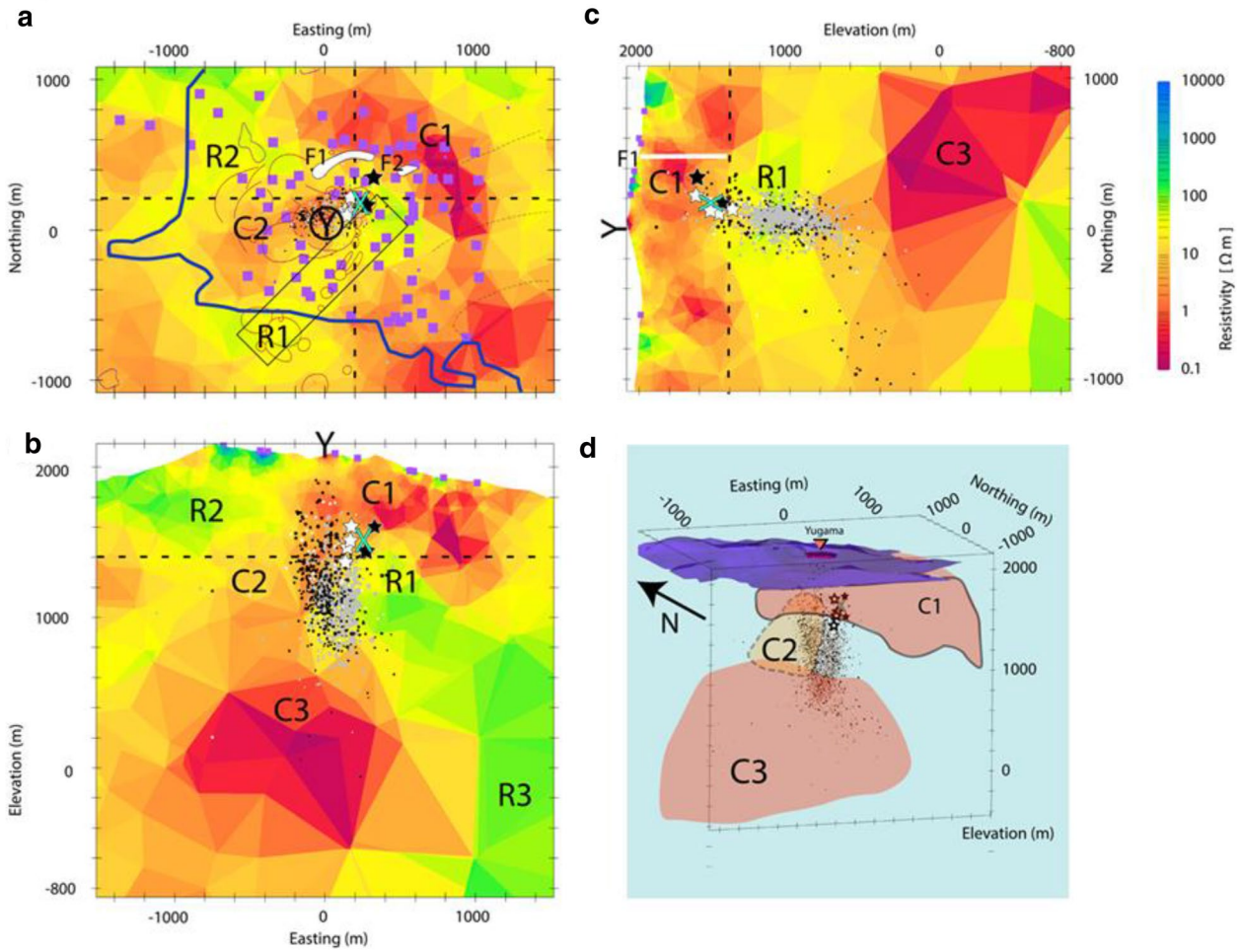

Fig. 4 **a** Depth slice at 1400 m ASL. The locations for W–E and S–N profiles for sections are shown by broken lines. **b** W–E and **c** S–N sections. The seismic hypocenters are mapped as dots on each map within 200 m tolerance normal to the sections. The white, black, and gray dots denote hypocenters before, during and after the 2014 unrest, respectively. The shallow seismicity (black dots) going through the clay cap (C1) is evident during the 2014 unrest. The white and black stars denote the same as in Fig. 3. The blue X denotes the point pressure source locations for explaining the radial infation of the edifce during the 2014 unrest (Terada et al. 2015). Two white masks with irregular shape in **a** denote the fumarole zone at the north of Yugama crater lake. The white line in **c** denotes the projection of fumarole zone F1 at 1400 m ASL. **d** The 3-D view of the three major conductors. The blue surface shows the topography. The dots denote seismicity as in **a**–**c**

We can also summarize the characteristics of the resistivity structure by sections (Fig. 4). Figure 4a shows the depth slice at 1400 m ASL, which is the same as Fig. 3b with locations for the EW (Fig. 4b) and NS (Fig. 4c) sections. From Fig. 4b and c, the existence of the two conductors is evident. One is the shallow conductor (1–10 Ωm) covering the eastern half of the peak area (C1). It has a bell shape whose center is shifted 400 m to the east from the center of the Yugama crater (Y), as seen in the EW and NS resistivity sections. The most active fumaroles in the northern edifice (F1 and F2) are located at the inner rim of the C1 conductor; however, these fumaroles do not show any other deeper features. The other conductor (C3) is a deep one located below 400 m ASL, which is beneath the Yugama crater and extends to the northwest (see also Fig. 3e). The Yugama crater is located at the edge of the C3. We can also see the subvertical conductor C2 in Fig. 4b at the western margin of the Yugama crater, which connects the deep (C3) and the shallow bell-shape (C1) conductors.

The resistive block (R1) starts to appear clearly at 1400 m (Fig. 4a). The shape of the R1 is elongated in the NE–SW direction to the east of the Yugama crater (*Y*), and the C1 conductor does not fully show an axially

symmetrical structure. This feature means that the clay cap is thin along with the R1 resistor.

Figure 4b section shows that the R1 resistor is covered by the clay cap (C1). We also see the resistive block (R3) to the east at depth, which needs to exist in order to explain the regional elongated phase tensor ellipse at low frequencies around 0.3 Hz (Fig. 2). In the NS section (Fig. 4c), we can also see the shallow bell-shaped conductor (C1) above 1400 m ASL, and the deep conductor (C3) below 400 m ASL. The seismicity is located between these deep and shallow conductors.

We tested the existence of C2 conductor, which connects C1 and C3 to the west of the Yugama crater (Additional file 2: Figure S17). The dotted block volume (ModC2 in Additional file 2: Figure S17) was replaced by 100 Ωm and resistivity contrast between C2, R1 and R2 are lost. The test model (ModC2) disconnects the deep conductor and the shallow bell-shaped conductor. The final RMS increased from 1.20 to 1.38. The phase tensors at 4.4 Hz clearly show a significantly worse fit at the sites at the southwest of the Yugama crater (Y) (Additional file 2: Figure S18c). This change in the phase tensor plot is more evident than the sounding curves (Additional file 2: Figures S19 and S20), but the deviation of apparent resistivity is still distinguishable. Therefore, the existence of C2 between the bell-shaped conductor (C1) and the deep conductor (C3) was confirmed.

Next, we tested the existence of the C3 conductor by replacing the resistivity in the dotted block volume (ModC3 in Additional file 2: Figure S17) with 50 Ωm. The RMS increased from 1.20 to 1.34, and a significantly worse fit is also seen in Additional file 2: Figure S18d at 1.1 Hz, where the calculated phase tensors from the test model response show lower $\mathbf{tan}^{-1}(\mathbf{\Phi}_2)$ phases at the northwest of Yugama crater than those observed (Additional file 2: Figure S18a). The response sounding curves represent a significant divergence between the best final model and test model (Additional file 2: Figures S21, S22). Thus the existence of C3 is confirmed.

Discussion

Clay–cap conductor (C1) and inner resistor (R1)

The distribution of the shallow conductor (C1) was also imaged previously by Nurhasan et al. (2006) and Matsunaga et al. (2020) on the eastern slope of the volcano. By reference to the drill hole data, they interpreted the conductor as a layer containing clay (smectite), which has low permeability as well as high electrical conductivity. In this paper, the distribution of the clay cap around the Yugama crater was imaged in detail, and it was found to be nearly bell shaped. These capping structures, the hydrothermal alteration products, are commonly found in geothermal areas (e.g., Heise et al. 2008; Yamaya et al. 2013; Seki et al. 2015; Piña-Varas et al. 2018; Yoshimura et al. 2018; Kanda et al. 2019). The bottom of the C1 smectite clay conductor is interpreted as the isotherm of 200 °C. The R1 resistor below C1 implies the smectite–illite transformation above 200 °C (Ussher et al. 2000).

We can compare the distribution of C1 with seismicity. The hypocenters were relocated using the best fitting seismic velocity model with the seismic monitoring data, including three borehole seismograms surrounding the Yugama crater within 500 m distances (See Additional file 2: Text S2–S4for details). As seen in the resistivity sections (Fig. 4b, c), most of the hypocenters are located below C1 conductor. This feature implies that the rising fluids increase the pore pressures and induce the microseismicity. However, the flow is inhibited by the low-permeability clay cap below the Yugama crater (Fig. 4b, c). Few earthquakes occurred inside the clay cap (C1) during the 2014 unrest. This may imply that fluids invaded into the clay cap during the 2014 unrest and supplied volcanic fluids into the crater lake Yugama.

Takahashi and Fujii (2014) analyzed the temporal variations of total magnetic intensity data from 1982 to 2012 and inverted the corresponding magnetization and demagnetization dipole locations to explain the temporal variation of temperature changes underneath the volcano. The magnetization and demagnetization source locations are also plotted in Fig. 4a, b by black and white stars, respectively. In the sections, the black and white stars are located near the R1 and C1 boundaries. This feature indicates that in the active period of the volcano, the high-temperature fluid reaches the bottom of the low-permeability clay cap (C1) and may partly intrude into the clay cap during the past unrests.

Nakano et al. (2003) modeled the long-period volcanic tremors during volcanic unrest (during the 1990s) at the Kusatsu–Shirane volcano and inferred a horizontal crack resonator which is located 300 m below Yugama crater. This inferred resonator is also located consistently with the demagnetization/magnetization sources, just below the clay cap at the top of R1 resistor.

During the 2014 unrest, we observed the radial inflation of the edifice by using three borehole tilt-meters surrounding the Yugama crater, simultaneously with the onset of increased seismicity (Terada et al. 2015). The location of the causative point source of inflation is indicated by the green "X" in Fig. 4a–c (Terada et al. 2015). The inflation source is located just below the clay cap at the northeastern edge of the Yugama crater. The inflation source will be interpreted by a supply of high-pressure volcanic hydrothermal fluid. Tsukamoto et al. (2018) also show a similar high-pressure source at Kirishima volcano, which lead the precursor of a phreatic eruption.

As seen in Fig. 3b, the resistive area of R1 starts to spread horizontally inside the C1 conductor as the radius of C1 increases with depth until the C1 becomes less significant at 1000 m ASL. The resistor implies a higher temperature zone where the smectite will become unstable and be converted to illite, which is electrically more resistive (Eberl 1978; Inoue et al. 1992). R1 is not circularly distributed symmetrically with Yugama but is elongated in the NE to SW direction. R1 follows the distribution of the historical phreatic eruption craters of 1902, 1932, and 1942, whose shapes are sketched in Figs. 3b and 4a (Terada, 2018). R1 breaks the circular symmetry of C1 conductor. The past phreatic eruptions may have destroyed the symmetric clay cap structure.

Brine conductor (C3)

A significant conductor (C3) with a resistivity less than 1 Ωm appears at 400 m ASL below the Yugama crater and extends to the northwest (Fig. 3d, e and Fig. 4b, c). The cutoff depth of microseismicity coincides with the bottom of C2, and the top of C3 conductor corresponds to brittle–ductile transition at around 400 °C. This conductor will be interpreted as brine above 400 °C, which will be separated from the magmatic fluids (Fournier 1999; Afanasyev et al. 2018). The top of the C3 fluids will be self-sealed by silica (Saishu et al. 2014) or by halite (Afanasyev et al. 2018), which can last for several hundred thousand years. The seal on top of C3 will separate the hydrostatic domain and underlying the lithostatic domain. The episodic supply of magmatic fluids or gas to C3 from below will increase the internal pressure of C3. The part of the seal will break and released fluids will increase the pore pressure in the overlying hydrostatic domain and will induce microseismicity.

Such conductors below the seismogenic zones are commonly found in volcanic regions and also under the seismically active regions (e.g., Ogawa et al. 2001, 2014; Wannamaker et al. 2009; Ichihara et al. 2014, 2016).

Vertical conductor (C2) connecting the brine (C3) to the surface (C1)

We also found a vertical conductor (C2) that connects the deep brine conductor (C3) to the clay cap rock conductor (C1). It can be regarded as a part of the deep extension of C1 conductor, but at 1000 m ASL, C1 conductor almost disappears, but C2 exists. It is also connected to the deeper conductor C3. Thus it is difficult to interpret C2 as the extension of smectite clay cap (C1), which must be lsss than 200 °C. This vertical conductor appears at around 1000–1400 m ASL (Fig. 3b, c), which is significantly deeper than C1 clay cap, and is associated with the microseismic hypocenters.

The microseismic activities can be interpreted as the fluid-induced swarm earthquakes when the overpressured fluid was invading into the fracture in the structure and diffusing, which is a typical feature in the volcanic hydrothermal system (Yukutake et al. 2011). The fracture in this structure can provide the fluid pathway and can reduce the bulk resistivity, although the rock porosity is decreased (e.g., Vidal et al. 2018). The vertical conductor C2 is interpreted as a conduit pathway of fluids from the deep brine reservoir to the surface. Similar vertical conductors connecting the deep reservoir to the surface were also suggested for other volcanoes (Seki et al. 2015; Tsukamoto et al. 2018). The invaded and diffused fluid made the structure seismogenic. When the volume of upward-invaded fluid was significant, or the pressure was relatively high, it induced the detectable microseismic activity (in this study, the threshold magnitude was − 3.0).

Conversely, when the fluid diffused in the structure with relatively lower volume and pressure, the microseismic activity could be too small to be detected. This difference could explain why the conductor C2 is not fully overlapping with the swarm plot of microseismic hypocenters in Fig. 4b. It also explains the occurrence of shallow seismic activity during 2014 unrest, because the volume of upward-released fluid increased then the fluid-induced microseismic activity became detectable.

Figure 4d represents the 3-D cartoon of the hydrothermal system of Kusatsu–Shirane volcano. The clay cap C1 located around the Yugama crater lake appeared in a bell shape and overlying the microseismic hypocenters. The microseismic hypocenters that indicated the major fluid pathway invaded upward. The fluid-filled fractured structure C2 is underlain by the clay cap C1. The brine reservoir C3 provides the filling hydrothermal fluid. The fluid released from this deep reservoir flow upward through the pathway conduit C2 to the surface supported the whole hydrothermal system of the Kusatsu–Shirane volcano.

Figure 5 demonstrates the phase transition of the released fluid using the diagram of Hutnak et al. (2009). We utilized the depth of microseismic swarm to speculate the bottom of the fluid pathway in the brittle–ductile transition zone (1400 m depth, 400 °C). We also utilized the bottom of C1 clay cap (400 m depth, 200 °C) (Fig. 5a). The phase transition between these two points is represented in the H_2O–CO_2 coexisting phase diagrams (Fig. 5b). We think that C2 is an established fluid pathway from the brine. In contrast, the seismicity above the bine may be induced by breaking the silica cap due to the over-pressure caused by an episodic large flux of magmatic gas, such as CO_2. This interpretation follows the porphyry model of Blundy et al. (2015). When the

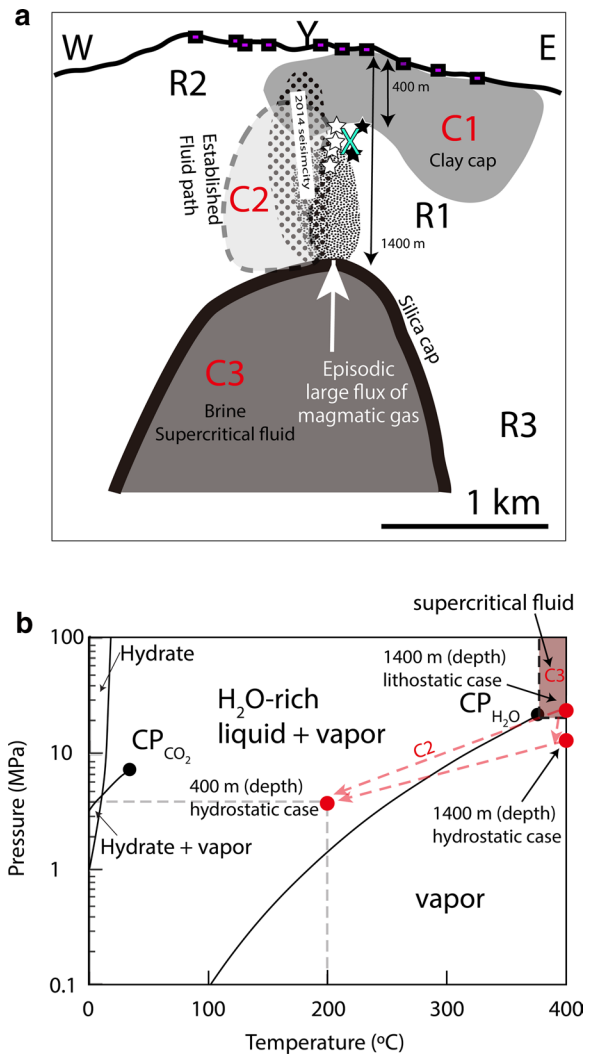

Fig. 5 **a** Simplified W–E resistivity section in Fig. 4b. The rectangles on the terrain denote the observation sites. The white and black stars and the green "X" symbols are the same as in Fig. 4. The swarm dots with bigger and with smaller circles denote the hypocenters of microseismic events during 2014 unrest, and out of this active period, respectively. **b** Pressure–temperature projection of hydrothermal fluid phase diagram for H_2O and CO_2 (after Hutnak et al. 2009). Two curves which end with solid circles denote the liquid–vapor coexistence curves of pure CO_2 and pure H_2O with their critical points (CP). C2 may be an established fluid path from the supercritical fluid. In contrast, if episodic large gas flux breaks the silica cap, breakage of the silica cap may flush the fluid upward in the hydrostatic domain

silica cap is broken, the pressure will be decreased from lithostatic to hydrostatic and brine will be first vaporized (Weatherley and Henley, 2013). In a hydrostatic domain, the phase of fluid will transit from pure vapor to liquid–gas-mixed fluid during upward migration. The sudden increase in liquid–gas-mixed fluid underlain by the clay cap C1 can lead the phreatic eruption. Therefore, the resistivity of the fluid pathway conduit C2 and its surrounding space should be monitored for predicting the phreatic eruption in the future.

Conclusions

The magmatic hydrothermal system of Kusatsu–Shirane volcano was imaged by the three-dimensional magnetotelluric modeling. The final model showed the low-permeability clay cap as near-surface conductor (C1) and the brine reservoir as a deep conductor (C3) at a depth of 1.4 km from the surface. The magnetization/demagnetization sources of the past unrests and the inflation point source of the 2014 unrest are located just below the clay cap (C1). This evidence supports that C1 works as the cap structure of the hydrothermal system.

The resistor (R1) underneath the clay cap (C1) runs in NE–SW directions and destroys the radial symmetry of the clay cap, which suggests that the past phreatic eruptions may have broken part of the clay cap. The fluid path from the C3 reservoir to the surface was imaged by a vertical conductor (C2). In contrast, the episodic magmatic gas flux may break the silica cap over the brine reservoir and vapor and the magmatic gas will be flushed into the hydrostatic domain and will induce seismicity during migration to the bottom of the clay cap.

The resistivity model provides the comprehension of the dynamics of the magmatic hydrothermal system beneath Kusatsu–Shirane volcano.

Abbreviations

MT: Magnetotelluric; AMT: Audio-magnetotelluric; RMS: Root-mean-square; ASL: Above sea level.Supplementary information

Supplementary information accompanies this paper at https://doi.org/10.1186/s40623-020-01283-2.

Additional file 1: Table S1. The site locations, altitude and magnetic field site which was used for the calculations of the impedances.

Additional file 2: Text S1. Definition of the error floor. **Text S2.** Information of microseismicity data. **Text S3.** Observed and calculated data with its location on the map (Figure S2–S16). **Text S4.** Sensitivity tests of the conductors C2 and C3 (Figure S17–S22). **Figure S23.** Deeper conductive feature beneath Kusatsu–Shirane volcano. **Figure S24–S26.** The seismic hypocenters before 2014 unrest mapping with **a** Depth slice at 1400m ASL **b** W–E and **c** S–N sections.

Acknowledgements

We thank Grant Caldwell for fruitful discussions for modeling. The constructive comments from Koki Aizawa and an anonymous reviewer improved the manuscript.

Authors' contributions

YO designed the magnetotelluric field survey and supervised the research. KHT performed the 3-D inversion. KHT and YO made interpretations. N and

SBT made preliminary magnetotelluric modelings. YO, N, SBT, NU, YH carried out magnetotelluric data acquisitions. AT provided seismic data, YU and WK contributed in the 3-D inversion. All authors read and approved the final manuscript.

Funding
This study was supported by the Ministry of Education, Culture, Sports, Science and Technology (MEXT) of Japan, under its Earthquake and Volcano Hazards Observation and Research Program. Iw was also supported by Grant-in-Aid for Scientific Research KAKENHI 20H01992.

Availability of data and materials
The data is available upon request to the corresponding author.

Competing interests
The authors declare that they have no competing interests.

Author details
[1]Department of Earth and Planetary Sciences, Tokyo Institute of Technology, Tokyo, Japan. [2]Volcanic Fluid Research Center, Tokyo Institute of Technology, Tokyo, Japan. [3]Present Address: Physics Department, Bandung Institute of Technology, Bandung, Indonesia. [4]Present Address: Boğaziçi University, Kandilli Obs. & E.R.I., Çengelköy, İstanbul, Turkey. [5]Present Address: Hydrographic and Oceanographic Department, Japan Coast Guard, Tokyo, Japan. [6]Present Address: Earthquake Research Institute, The University of Tokyo, Tokyo, Japan.

Received: 15 February 2020 Accepted: 28 September 2020
Published: 23 October 2020

References

Aizawa K, Ogawa Y, Ishido T (2009) Groundwater flow and hydrothermal systems within volcanic edifices: Delineation by electric self-potential and magnetotellurics. J Geophys Res Solid Earth. https://doi.org/10.1029/2008JB005910

Afanasyev A, Blundy J, Melnik O, Sparks S (2018) Formation of magmatic brine lenses via focussed fluid-flow beneath volcanoes. Earth Planet Sci Lett 486:119–128. https://doi.org/10.1016/j.epsl.2018.01.013

Blundy J, Mavrogenes J, Tattitch B, Sparks S, Gilmer A (2015) Generation of porphyry copper deposits by gas–brine reaction in volcanic arcs. Nature Geosci 8:235–240. https://doi.org/10.1038/ngeo2351

Caldwell TG, Bibby HM, Brown C (2004) The magnetotelluric phase tensor. Geophys J Int 158:457–469. https://doi.org/10.1111/j.1365-246X.2004.02281.x

Eberl D (1978) Reaction series for dioctahedral smectites. Clays Clay Miner 26:327–340. https://doi.org/10.1346/CCMN.1978.0260503

Fournier RO (1999) Hydrothermal processes related to movement of fluid from plastic into brittle rock in the magmatic–epithermal environment. Econ Geol 94:1193–1211. https://doi.org/10.2113/gsecongeo.94.8.1193

Heise W, Caldwell TG, Bibby HM, Bannister SC (2008) Three-dimensional modelling of magnetotelluric data from the Rotokawa geothermal field, Taupo Volcanic Zone, New Zealand. Geophys J Int 173:740–750. https://doi.org/10.1111/j.1365-246X.2008.03737.x

Herd DG (1986) The 1985 Ruiz Volcano disaster. Eos Trans Am Geophys Union 67:457. https://doi.org/10.1029/EO067i019p00457-03

Hutnak M, Hurwitz S, Ingebritsen SE, Hsieh PA (2009) Numerical models of caldera deformation: effects of multiphase and multicomponent hydrothermal fluid flow. J Geophys Res 114:B04411. https://doi.org/10.1029/2008JB006151

Ichihara H, Mogi T, Tanimoto K, Yamaya Y, Hashimoto T, Uyeshima M, Ogawa Y (2016) Crustal structure and fluid distribution beneath the southern part of the Hidaka collision zone revealed by 3-D electrical resistivity modeling. Geochem Geophys Geosyst 17:1480–1491. https://doi.org/10.1002/2015GC006222

Ichihara H, Sakanaka S, Mishina M, Uyeshima M, Nishitani T, Ogawa Y, Yamaya Y, Mogi T, Amita K, Miura T (2014) A 3-D electrical resistivity model beneath the focal zone of the 2008 Iwate-Miyagi Nairiku earthquake (M 7.2). Earth Planets Space 66:50. https://doi.org/10.1186/1880-5981-66-50

Inoue A, Utada M, Wakita K (1992) Smectite-to-illite conversion in natural hydrothermal systems. Appl Clay Sci 7:131–145. https://doi.org/10.1016/0169-1317(92)90035-L

Kanda W, Utsugi M, Takakura S, Inoue H (2019) Hydrothermal system of the active crater of Aso volcano (Japan) inferred from a three-dimensional resistivity structure model. Earth Planets Space 71:37. https://doi.org/10.1186/s40623-019-1017-7

Kaneko T, Maeno F, Nakada S (2016) 2014 Mount Ontake eruption: characteristics of the phreatic eruption as inferred from aerial observations. Earth Planets Space 68:72. https://doi.org/10.1186/s40623-016-0452-y

Kobayashi T, Morishita Y, Munekane H (2018) First detection of precursory ground inflation of a small phreatic eruption by InSAR. Earth Planet Sci Lett 491:244–254. https://doi.org/10.1016/j.epsl.2018.03.041

Martí A, Queralt P, Marcuello A, Ledo J, Rodríguez-Escudero E, Martínez-Díaz JJ, Campanyà J, Meqbel N (2020) Magnetotelluric characterization of the Alhama de Murcia Fault (Eastern Betics, Spain) and study of magnetotelluric interstation impedance inversion. Earth Planets Space 72:16. https://doi.org/10.1186/s40623-020-1143-2

Matsunaga Y, Kanda W, Takakura S, Koyama T, Saito Z, Seki K, Suzuki A, Kishita T, Kinoshita Y, Ogawa Y (2020) Magmatic hydrothermal system inferred from the resistivity structure of Kusatsu–Shirane Volcano. J Volcanol Geotherm Res 390:106742. https://doi.org/10.1016/j.jvolgeores.2019.106742

Nakano M, Kumagai H, Chouet BA (2003) Source mechanism of long-period events at Kusatsu–Shirane Volcano, Japan, inferred from waveform inversion of the effective excitation functions. J Volcanol Geotherm Res 122:149–164. https://doi.org/10.1016/S0377-0273(02)00499-7

Nurhasan, Ogawa Y, Ujihara N, Tank SB, Honkura Y, Onizawa S, Mori T, Makino M (2006) Two electrical conductors beneath Kusatsu–Shirane volcano, Japan, imaged by audiomagnetotellurics, and their implications for the hydrothermal system. Earth Planets Space 58:1053–1059. https://doi.org/10.1186/BF03352610

Ogawa Y, Mishina M, Goto T, Satoh H, Oshiman N, Kasaya T, Takahashi Y, Nishitani T, Sakanaka S, Uyeshima M, Takahashi Y, Honkura Y, Matsushima M (2001) Magnetotelluric imaging of fluids in intraplate earthquake zones, NE Japan Back Arc. Geophys Res Lett 28:3741–3744. https://doi.org/10.1029/2001GL013269

Ogawa Y, Ichiki M, Kanda W, Mishina M, Asamori K (2014) Three-dimensional magnetotelluric imaging of crustal fluids and seismicity around Naruko volcano NE Japan. Earth Planets Space 66:158. https://doi.org/10.1186/s40623-014-0158-y

Ohba T, Yaguchi M, Nishino K, Numanami N, Tsunogai U, Ito M, Shingubara R (2019) Time variation in the chemical and isotopic composition of fumarolic gasses at Kusatsu–Shirane Volcano, Japan. Front Earth Sci. https://doi.org/10.3389/feart.2019.00249

Piña-Varas P, Ledo J, Queralt P, Marcuello A, Perez N (2018) On the detectability of Teide volcano magma chambers (Tenerife, Canary Islands) with magnetotelluric data. Earth Planets Space 70:14. https://doi.org/10.1186/s40623-018-0783-y

Saishu H, Okamoto A, Tsuchiya N (2014) The significance of silica precipitation on the formation of the permeable–impermeable boundary within Earth's crust. Terra Nova 26:253–259. https://doi.org/10.1111/ter.12093

Sano Y, Hirabayashi J-I, Oba T, Gamo T (1994) Carbon and helium isotopic ratios at Kusatsu–Shirane Volcano, Japan. Appl Geochem 9:371–377. https://doi.org/10.1016/0883-2927(94)90059-0

Seki K, Kanda W, Ogawa Y, Tanbo T, Kobayashi T, Hino Y, Hase H (2015) Imaging the hydrothermal system beneath the Jigokudani valley, Tateyama volcano, Japan: implications for structures controlling repeated phreatic eruptions from an audio-frequency magnetotelluric survey. Earth Planets Space 67:6. https://doi.org/10.1186/s40623-014-0169-8

Stix J, de Moor JM (2018) Understanding and forecasting phreatic eruptions driven by magmatic degassing. Earth Planets Space 70:83. https://doi.org/10.1186/s40623-018-0855-z

Takahashi K, Fujii I (2014) Long-term thermal activity revealed by magnetic measurements at Kusatsu–Shirane volcano, Japan. J Volcanol Geotherm Res 285:180–194. https://doi.org/10.1016/j.jvolgeores.2014.08.014

Tazieff H (1989) Mechanisms of the Nyos carbon dioxide disaster and of so-called phreatic steam eruptions. J Volcanol Geotherm Res 39:109–116. https://doi.org/10.1016/0377-0273(89)90051-6

Terada A (2018) Kusatsu–Shirane volcano as a site of phreatic eruptions. J Geol Soc Japan 124:251–270. https://doi.org/10.5575/geosoc.2017.0060
Terada A, Morita Y, Hashimoto T, Mori T, Ohba T, Yaguchi M, Kanda W (2018) Water sampling using a drone at Yugama crater lake, Kusatsu–Shirane volcano, Japan. Earth Planets Space 70:64. https://doi.org/10.1186/s40623-018-0835-3
Terada A, Ohkura T, Kanda W, Ogawa Y (2015) Ground deformation caused by an accumulation of hydrothermal water beneath hot crater lake at Kusatsu– Shirane volcano. In: Abstracts of Japan geoscience union meeting 2015, Makuhari, Chiba, Japan, 24-28 May 2015.
Tsukamoto K, Aizawa K, Chiba K, Kanda W, Uyeshima M, Koyama T, Utsugi M, Seki K, Kishita T (2018) Three-dimensional resistivity structure of Iwo-Yama Volcano, Kirishima Volcanic Complex, Japan: relationship to shallow seismicity, surface uplift, and a small phreatic eruption. Geophys Res Lett. https://doi.org/10.1029/2018GL080202
Ussher G, Harvey C, Johnstone R, Anderson E (2000) Understanding the resistivities observed in geothermal systems. In: Proceedings world geothermal congress, Kyushu-Tohoku, Japan, 28 May–10 June 2000, pp 1915–1920
Usui Y (2015) 3-D inversion of magnetotelluric data using unstructured tetrahedral elements: applicability to data affected by topography. Geophys J Int 202:828–849. https://doi.org/10.1093/gji/ggv186
Usui Y, Ogawa Y, Aizawa K, Kanda W, Hashimoto T, Koyama T, Yamaya Y, Kagiyama T (2017) Three-dimensional resistivity structure of Asama Volcano revealed by data-space magnetotelluric inversion using unstructured tetrahedral elements. Geophys J Int 208:1359–1372. https://doi.org/10.1093/gji/ggw459
Vidal J, Patrier P, Genter A, Beaufort D, Dezayes C, Glaas C, Lerouge C, Sanjuan B (2018) Clay minerals related to the circulation of geothermal fluids in boreholes at Rittershoffen (Alsace, France). J Volcanol Geotherm Res 349:192–204. https://doi.org/10.1016/j.jvolgeores.2017.10.019
Wannamaker PE, Caldwell TG, Jiracek GR, Maris V, Hill GJ, Ogawa Y, Bibby HM, Bennie SL, Heise W (2009) Fluid and deformation regime of an advancing subduction system at Marlborough, New Zealand. Nature 460:733–736. https://doi.org/10.1038/nature08204
Weatherley D, Henley R (2013) Flash vaporization during earthquakes evidenced by gold deposits. Nature Geosci 6:294–298. https://doi.org/10.1038/ngeo1759
Yamaya Y, Alanis PKB, Takeuchi A, Cordon JM, Mogi T, Hashimoto T, Sasai Y, Nagao T (2013) A large hydrothermal reservoir beneath Taal Volcano (Philippines) revealed by magnetotelluric resistivity survey: 2D resistivity modeling. Bull Volcanol 75:729. https://doi.org/10.1007/s00445-013-0729-y
Yoshimura R, Ogawa Y, Yukutake Y, Kanda W, Komori S, Hase H, Goto T, Honda R, Harada M, Yamazaki T, Kamo M, Kawasaki S, Higa T, Suzuki T, Yasuda Y, Tani M, Usui Y (2018) Resistivity characterization of Hakone volcano, Central Japan, by three-dimensional magnetotelluric inversion. Earth Planets Space 70:66. https://doi.org/10.1186/s40623-018-0848-y
Yukutake Y, Ito H, Honda R, Harada M, Tanada T, Yoshida A (2011) Fluid-induced swarm earthquake sequence revealed by precisely determined hypocenters and focal mechanisms in the 2009 activity at Hakone volcano, Japan. J Geophys Res 116:B04308. https://doi.org/10.1029/2010JB00803

Publisher's Note